J Mater Sci (2021) 56:16726–16744

Metals & corrosion

Evolution of pitting corrosion resistance and mechanical properties in ultrafine-grained commercially pure aluminium during annealing

Marta Orłowska[1,*], Ewa Ura-Bińczyk[2], Bogusława Adamczyk-Cieślak[2], Lech Olejnik[3], and Małgorzata Lewandowska[2]

[1] Faculty of Mechanical Engineering, Military University of Technology, Gen. S. Kaliskiego 2, 00-908 Warsaw, Poland
[2] Faculty of Materials Science and Engineering, Warsaw University of Technology, Wołoska 141, 02-507 Warsaw, Poland
[3] Faculty of Production Engineering, Warsaw University of Technology, Narbutta 85, 02-524 Warsaw, Poland

Received: 7 May 2021
Accepted: 16 July 2021
Published online: 28 July 2021

© The Author(s) 2021

ABSTRACT

The aim of the present study was to determine the evolution of resistance to pitting corrosion and changes in the mechanical properties of ultrafine-grained aluminium during annealing. In contrast to the numerous papers devoted to the topic of the corrosion resistance of severely deformed aluminium alloys, a unique approach has been taken in this study. The size and distribution of the primary intermetallic particles, which are crucial in terms of corrosion resistance, remain constant during annealing. Therefore, the influence of other microstructural features could be investigated and compare with the results of mechanical properties. It was shown that the ultrafine-grained structure of commercially pure aluminium was stable up to 200 °C. Higher annealing temperatures caused significant grain growth and a reduction in dislocation density, which resulted in a drop in mechanical strength. Also, the corrosion resistance slightly decreased, since with an increase in annealing temperature a decrease in the corrosion potential, pit size, and the area damaged by corrosion attack were noted. The best combination of mechanical strength and resistance to pitting corrosion has been achieved for as-deformed state.

Introduction

The unique properties of ultrafine-grained (UFG) materials, which arise from their refined microstructures, make them of great interest [1]. The major improvement in UFG materials, in comparison with coarse-grained (CG) ones, is enhanced mechanical strength caused by grain boundary- and dislocation strengthening mechanisms [2]. However, due to the elevated amount of structural defects and strain accumulated during plastic deformation, such

Handling Editor: Sophie Primig.

Address correspondence to E-mail: marta.orlowska@wat.edu.pl

https://doi.org/10.1007/s10853-021-06355-6

materials have low thermal stability [3, 4]. UFG materials have a large amount of stored energy after severe plastic deformation (SPD) processing [5], which reduces the necessary energy for grain growth activation. Annealing at elevated temperatures leads to grain growth, which can be very rapid, depending on the temperature. Therefore, every benefit that comes from a small grain size, mainly mechanical strength, decreases. The rate of the changes depends on the material, e.g. the purity level and microstructure, but also the temperature and annealing time.

In contrast to the mechanical strength, the correlation between grain size and corrosion resistance is still not clearly defined. It was shown in a review paper covering a wide range of metals and their alloys [6] that grain refinement, which causes changes in the reactivity of a material's surface, influences the corrosion response. The particular combination of corrosion environment, processing, and material will determine whether the increased surface reactivity will lead to either enhanced dissolution or faster passivation, so each material should be considered separately. It was shown [6] that grain refinement appears to increase the corrosion resistance of Mg and Ti alloys. However, for other material systems reviewed in that paper, the influence was not as clear cut, appearing to cause both increased and decreased corrosion susceptibility, depending on other factors, such as material processing and the corrosion environment.

In UFG materials, an improvement in passivation behaviour has been claimed to be due to the increased number of grain boundaries and dislocations, which act as active sites for passive film nucleation [7–10]. The multiplication of these sites enhanced the passivation ability of the material [9, 11, 12]. Therefore, a number of papers, e.g. [13, 14], show that UFG microstructure caused the formation of a denser and more uniform passive layer, thereby enhancing corrosion-protective properties. Nevertheless, corrosion processes are complex, and not only grain size, but also other microstructural factors, such as grain size distribution [15], grain boundary character [16], and strain localization [17, 18], contribute to the corrosion properties. Therefore, depending on the investigated material and its microstructural features, SPD processing can also have a negligible or negative impact on corrosion resistance [19] or change the corrosion response [20]. Additionally, the presence of a second phase or intermetallic particles significantly influences the corrosion resistance by the formation of galvanic couplings between the particles and the matrix due to changes in electrochemical potential. Therefore, the vicinities of such particles are sites of pitting corrosion initiation [21]. In age-hardenable Al alloys, SPD processing causes a fragmentation or a more uniform distribution of intermetallic and second-phase particles [22]. Commercially pure aluminium also contains particles; in this case they are called primary intermetallic particles, and they are mainly rich in Si [23] or arise from the ternary Al–Fe–Si system [24]. The fragmentation of intermetallic particles during SPD processing can contribute to an improvement in corrosion resistance [25], due to the formation of a more stable passive film and a reduction in microgalvanic currents [23, 26]. On the other hand, an increased number of particles due to SPD processing may result in an increase in the corrosion rate due to the elevated number of pit initiation sites, as was shown for commercially pure aluminium after equal channel angular pressing (ECAP) [26] or AA6061 after cold drawing [27], both of which were examined in NaCl solution.

The aim of the present study was to investigate the changes in microstructure of severely deformed commercially pure aluminium with subsequent annealing and correlate them with changes in mechanical properties and resistance to pitting corrosion. The material was initially severely deformed in order to refine the microstructure, but in contrast to other studies, the influence of grain size on corrosion resistance was investigated through annealing. Because of this procedure, as the size and distribution of the primary intermetallic particles remained constant, the influence of other microstructural features could be investigated. In the majority of studies, SPD processing led to the fragmentation of such particles, which have a more significant influence on corrosion resistance than does grain size. In the present study, the methodology used allowed a focus on other microstructural factors, as the impact from intermetallic particles was constant. The objectives of this study were to investigate and optimize the correlations between microstructure, mechanical properties, and corrosion resistance.

Materials and methods

Materials

The investigated material was commercially pure aluminium AA1070 aluminium (min. 99.70 wt% of Al). As an SPD method, multi-turn equal channel angular pressing (mtECAP) with two parallel channels [28] was chosen. The starting material, in the form of a bar with a diameter of ø38 mm, was subjected to machining, as a result of which mtECAP billets were obtained. The billets with dimension of 26 × 26 × 130 mm were subjected to a chemical process consisting of cleaning, degreasing, pickling, conversion coating and putting a lubricant layer (soap). The detailed procedure has been described in [29]. This scheme was repeated after each pass. A channel with 2 × 90° angular angles was used [30]. The modified B_C deformation path was used, i.e. the billet was rotated between two successive passes by 90°. During one pass, when passing between angular channels, the billet was rotated by 180° in the die, which is equivalent to deformation path *C* [31]. Thus, the final deformation path was $C + B_C$. The scheme of the process together with a chosen deformation route is illustrated in Fig. 1. Four passes were performed, which corresponded to an accumulative deformation strain $\varepsilon = 9.2$.

Samples were investigated in the initial (deformed) state and after annealing. Annealing was performed at four temperatures: 100 °C, 200 °C, 300 °C, and 400 °C. In each case the annealing time was 1 h. This process allowed samples to be obtained that varied in their microstructure, mainly with regard to grain size, dislocation density, and fraction of low- and high-angle grain boundaries (LAGBs and HAGBs, respectively). Samples were investigated in terms of their mechanical properties, corrosion resistance, and the dependence of these properties on the microstructural changes caused by the annealing. All examinations were performed on plane *Y* (the flow plane) according to ECAP notation [32].

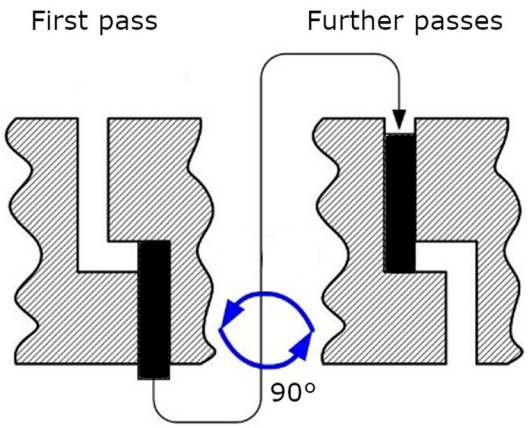

Figure 1 The scheme of applied mtECAP process with rotating the batch by 90° between passes.

Microstructure characterization

Microstructure observations were performed using a Hitachi SU-70 scanning electron microscope (SEM). Observations were made in secondary electron mode along with an analysis of the chemical composition of the particles of the primary intermetallic phases using an EDX detector. In addition, analyses were performed using an electron backscatter diffraction (EBSD) detector, which allowed the average grain size (d), expressed as equivalent diameter (diameter of a circle having the same area as the examined grain), to be determined; both LAGBs (misorientation angle $3° \le \varphi \le 15°$) and HAGBs (misorientation angle $\varphi > 15°$) were taken into account for this measurement, and the fraction of high-angle grain boundaries (%HAGBs) was determined. Also, S_V factor has been determined, which describes the ratio between the area covered by grain boundaries and unit volume. Furthermore, in order to examine microtexture the inverse pole figures (IPF) have been determined and analysed. Observations were conducted on samples in the form of thin foil. Samples were initially ground with SiC abrasive paper, with subsequent electropolishing on a Struers TenuPol5 electropolisher at a temperature of 5 °C and a voltage of 35 V in a solution made up of ethanol, perchloric acid, butyl glycol, and distilled water. EBSD maps were constructed with a 150-nm step size for each sample, choosing representative areas for presentation. For detailed microstructure investigation, observations were carried out using a JEOL JEM-1200 transmission electron microscope, with thin foil being prepared as for the EBSD measurements.

Measurements of the dislocation densities before and after annealing were performed by X-ray diffraction (XRD) at room temperature using a Bruker D8 Advance diffractometer with filtered CuKα ($\lambda = 0.154056$ nm) radiation. The conditions were as follows: voltage = 40 kV, current = 40 mA, angular range of 2θ from 30 to 110°, step $\Delta 2\theta = 0.025°$, and

counting time per step = 4 s. Finally, the dislocation density ρ was calculated from XRD peak broadening using the modified Williamson-Hall plot [33]:

$$\rho = 14.4 \cdot \varepsilon^2 / b^2$$

where b is the Burgers vector (b = 0.286 nm for aluminium) and ε is the lattice strain.

Mechanical testing

The mechanical properties were tested by microhardness measurements and tensile tests. Microhardness measurements were taken on prepared metallographic specimens on a Falcon 500 hardness tester. The Vickers method was applied, with a load of 200 g. For each sample, a minimum of five measurements were taken. Static tensile tests were performed on flat mini-samples with a cross section of 0.6 × 0.8 mm and a gauge length of 5 mm [34]. The strain rate was 10^{-3} s^{-1}. Digital image correlation (DIC) was used for contactless determination of strain. From tensile tests, the ultimate tensile strength (UTS), yield stress (YS), and the elongation to failure (E) were calculated. Three measurements were taken for each set of conditions, and the results presented were the average values obtained from the tests. Fractures present after the tensile tests were observed on a Hitachi SU-70 scanning electron microscope.

Electrochemical testing

Electrochemical tests were preceded by the preparation of samples by mechanical grinding using SiC abrasive paper in gradations of up to #4000. Samples were then degreased in an ultrasonic washer in ethanol. Corrosion resistance was estimated based on potentiodynamic polarization (PP) tests carried out in 3.5 wt% NaCl at ambient temperature (21 °C) in a Faraday cage, which allowed electromagnetic noise from the environment to be cut out. Electrochemical measurements were carried out on an Autolab PGSTAT 32 N device with a three-electrode system. The tested material was the working electrode, a platinum wire was the counter electrode, and a silver chloride ($Ag|AgCl|Cl^-$) electrode was the reference electrode. The PP tests were carried out with a scan rate of 1 mV/s. The scans were repeated for each sample at least five times to ensure the reproducibility of the results. Example curves are presented for each state. After the potentiodynamic polarization tests, samples were rinsed with ethanol, and then their surface was observed using SEM in order to analyse its post-corrosion morphology. Two quantitative parameters of corrosion attack were calculated—d_p [μm], which is the average size of the pit, and A_A [%], which is the surface area attacked by corrosion in relation to the unit surface area.

Results

Microstructure

Grain size, grain boundaries orientation, and dislocation density

The orientation maps (OIMs) from the EBSD analysis are presented in Fig. 2, while the average values of grain size and the fraction of HAGBs are listed in Table 1. After the mtECAP process, the microstructure consisted of grains with an average size of 1.3 μm and a fraction of HAGBs close to 60%. Annealing up to a temperature of 200 °C only caused a minor change in the microstructure, as the average grain size increased slightly (from 1.3 to 1.5 μm), and the differences between the samples were within the error limits. However, there was a continuous increase in the fraction of HAGBs. Annealing at 300 °C caused a significant increase in the average grain size to a value of approx. 10 μm, while increasing the annealing temperature to 400 °C caused a further increase in this parameter up to 14 μm. For the temperatures of 300 °C and 400 °C there was a significant spread in the results, which indicated selective grain growth during annealing. As the annealing temperature increased, the fraction of grain boundaries with a high misorientation angle also increased. In order to comprehensively describe the microstructure, the S_V factor was evaluated for all grain boundaries, as well as for LAGB and HAGB separately. The results are shown in Fig. 3. The total value of S_V increased slightly for annealing at 100 °C and then decreased for 200 °C to a value of 0.7 μm^{-1}. For higher temperatures, the decrease was significant, reaching a value of 0.1 μm^{-1}. This decrease indicated that the surface covered by grain boundaries was seven times smaller after annealing at 300 °C and 400 °C in comparison with the as-deformed sample. Regarding the grain boundaries'

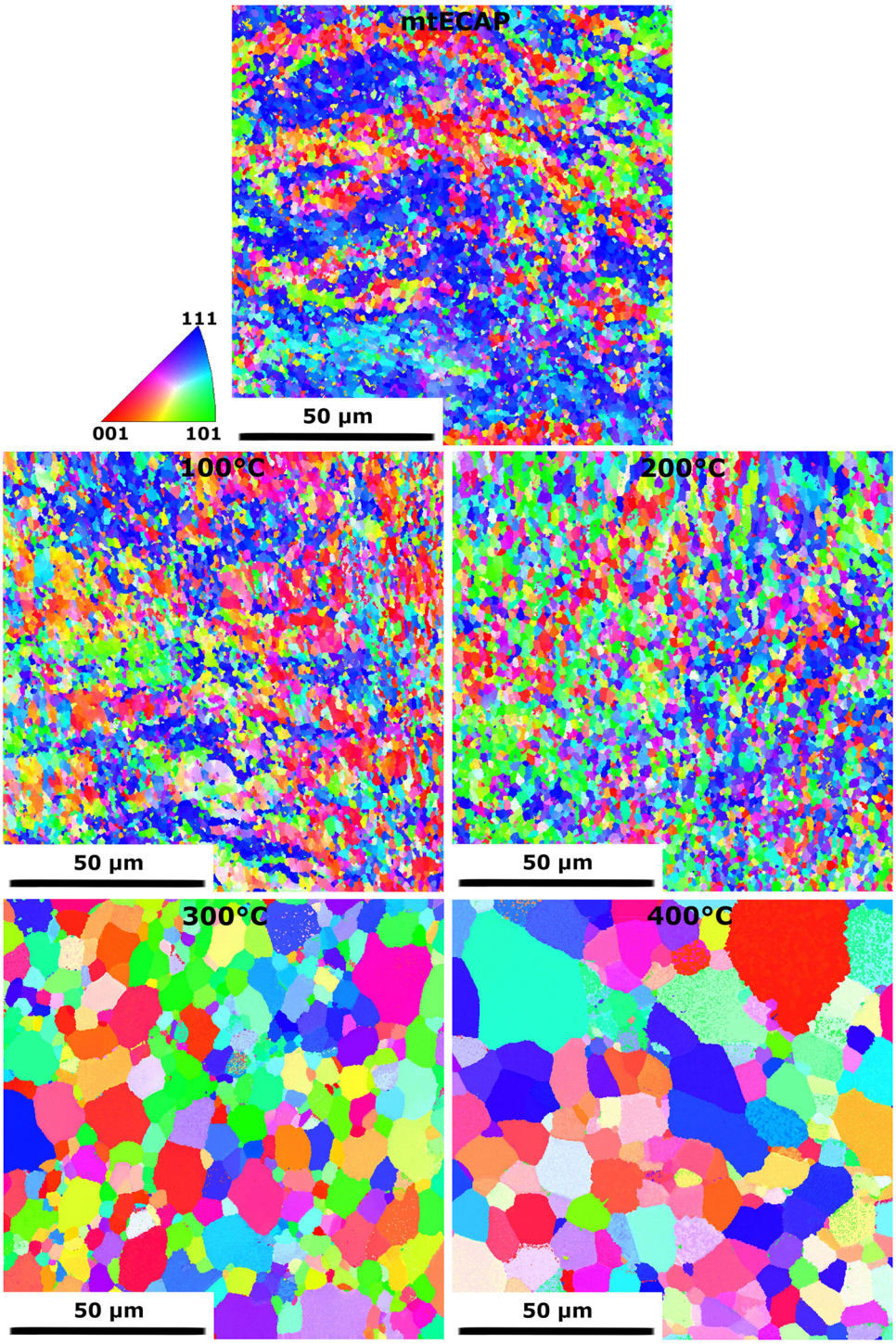

Figure 2 OIMs of sample after the mtECAP process and subsequent annealing.

misorientation angle, the S_V factor for LAGB decreased continuously, with a more significant decrease between 200 and 300 °C. For HAGB the value of S_V increased initially, and an abrupt drop before 300 °C was observed.

IPFs are shown in Fig. 4, where changes in grains orientation during annealing can be observed. For initial samples, grains have < 122 > orientation. However, it has to be noted that texture intensity is not significant. Annealing process causes the change in preferred orientations. For 200 °C, the grains are oriented in < 101 > direction. The most distinguishable change in grains orientation has been observed between temperature 200 and 300 °C. For the latter

Table 1 The results of the average grain size (d) and fraction HAGBs for AA 1070 after the mtECAP process and subsequent annealing

	mtECAP	100 °C	200 °C	300 °C	400 °C
d [μm]	1.30 ± 0.64	1.28 ± 0.74	1.47 ± 0.74	10.43 ± 3.33	14.31 ± 5.55
HAGB [%]	59.4	65.0	68.7	71.8	72.9

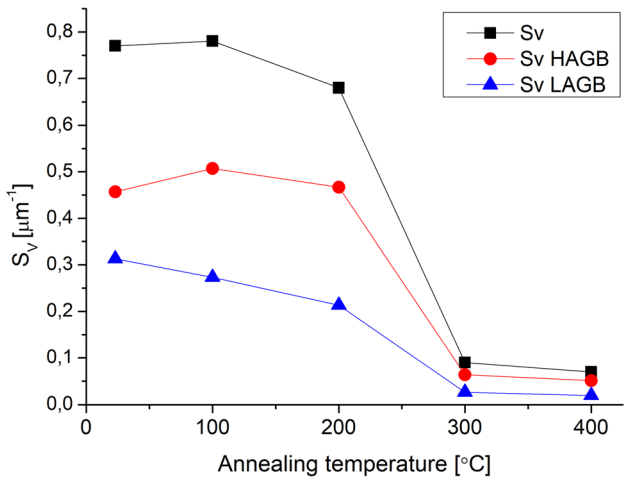

Figure 3 Graph of the dependence of the coefficient S_V on annealing temperature.

one, the grains have < 112 > orientation and it remains preserved for 400 °C. What is also noticeable is the constant increase in the intensity of texture with increasing the annealing temperature.

For detailed microstructure characterization, TEM observations were conducted, and examples of micrographs are shown in Fig. 5. The initial microstructure (Fig. 5a) was typical for Al after SPD processing. Grain refinement occurred by the extension and compression of grain boundaries with strain (successive mtECAP passes), combined with grains being subdivided by new HAGBs being formed discontinuously, on a finer and finer scale, until ultimately a limit was reached where the HAGB spacing converged with the subgrain size [35]. In addition, deformed grains with a size below 1 μm and with well-defined HAGBs, along with dislocation boundaries, could be observed. The achieved average grain size was above 1 μm, despite the large applied strain. The relatively high grain size was caused partly by the purity level of the aluminium, but also by its low homologous temperature and the low content of other elements, such as Mg, which could lower stacking fault energy and inhibit recovery [36]. Numerous dislocation lines and tangles could be observed (examples marked by white arrows). Annealing at 100 °C and 200 °C did not significantly influence the average grain size; however, for 200 °C (Fig. 5c) a considerable decrease in dislocation density could be observed in comparison with the initial sample and that annealed at 100 °C. Annealing at 300 °C caused significant grain growth. Nevertheless, this growth was selective, as some grains remained with a size of 1–2 μm. Annealing at 400 °C caused further grain growth.

The density of the dislocations was determined from XRD measurements. The results are presented as a graph in Fig. 6. For the initial material after the mtECAP process, a high density was observed (4.7×10^{13} cm^{-2}). After annealing, this value decreased in an almost logarithmic manner, which was indicated by the highest drop being at the very beginning, for 100 °C, while the subsequent decrease was less abrupt. After annealing at 400 °C, the dislocation density equaled 9.2×10^{12} cm^{-2}.

Intermetallic particles

The SEM micrographs showing the microstructure of the sample after mtECAP and with subsequent annealing at 400 °C are shown in Fig. 7. The size, distribution, and composition of the primary particles of the intermetallic phase (seen as white dots and indicated by arrows) did not change as a result of annealing. The results of the chemical composition of EDX analysis for an exemplary particle marked by a red arrow are shown in Fig. 7c. The results reveal that the particle is rich in Al, Fe, and Si. The great majority of present particles were α-AlFeSi; however, there were also some Al_3Fe phases, which is commonly observed in commercially pure aluminium. Their size did not exceed 4 μm, and their arrangement was random, without any preferred locations. In the deformed materials, deformed areas could be observed in the vicinity of such particles and this arrangement has been investigated in the literature, e.g. for cold-rolled commercially pure aluminium [37]. The contribution to the mechanical strength of such particles is negligibly small and will not be considered in the present study. However, such particles play a considerable role in corrosion resistance.

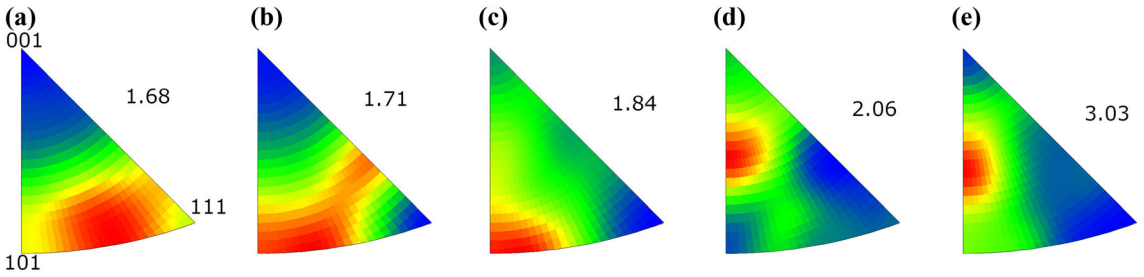

Figure 4 IPF of samples after: **a** mtECAP process and subsequent annealing for 1 h at **b** 100 °C, **c** 200 °C, **d** 300 °C, and **e** 400 °C, with distinguished maximum intensity.

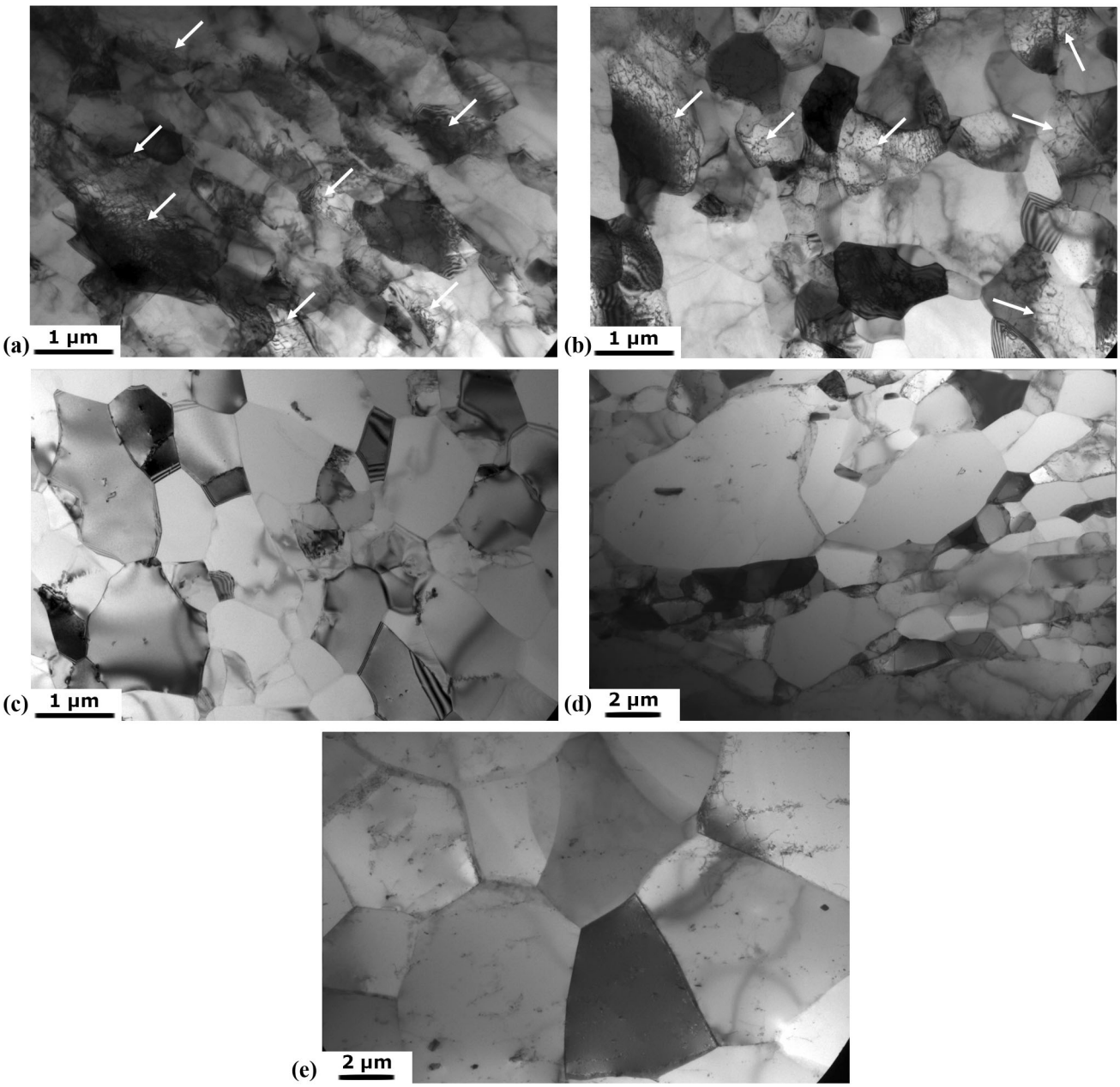

Figure 5 TEM micrographs of sample after **a** mtECAP and with subsequent annealing at **b** 100 °C, **c** 200 °C, **d** 300 °C, **e** 400 °C; arrows indicate dislocations.

Mechanical properties

The graph presenting the results for the dependence of microhardness on annealing temperature is shown in Fig. 8. The microhardness of annealed commercially pure aluminium, depending on the purity level, is estimated to be about 20–25 HV0.2. After the mtECAP process, the microhardness equaled about 46 HV0.2, which is almost a twofold increase. It can be seen that annealing up to 200 °C did not cause any significant changes in the microhardness, and the observed differences were within the error limit. At a temperature of 300 °C, there was a sharp drop to approximately 25 HV0.2. Higher annealing temperature resulted in a further decrease in microhardness: after annealing at 400 °C, the microhardness decreased to about 22 HV0.2.

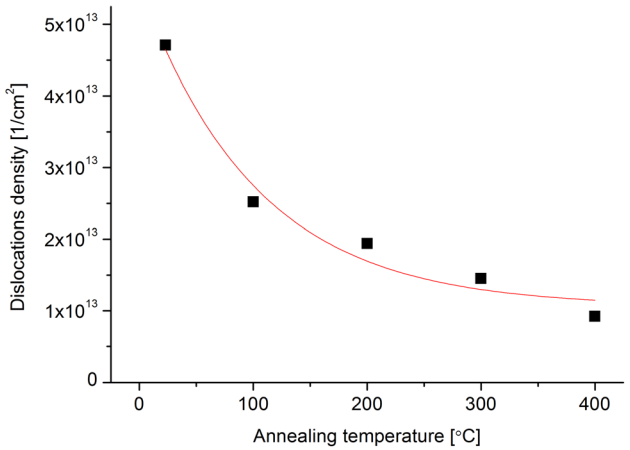

Figure 6 The dependence of dislocation density on annealing temperature.

Representative curves obtained from the tensile tests are shown in Fig. 9a, while a graph presenting the dependence of the average values of YS, UTS, and E on annealing temperature is shown in Fig. 9b. The tensile curves for the sample after the mtECAP process and for those that underwent a subsequent annealing at 100 °C or 200 °C were similar—the stress quickly achieved a maximum value and then decreased. These were typical curves for cold-worked metals. For samples annealed at higher temperatures, the stress increased gradually and as a result, much higher elongations at break values were achieved.

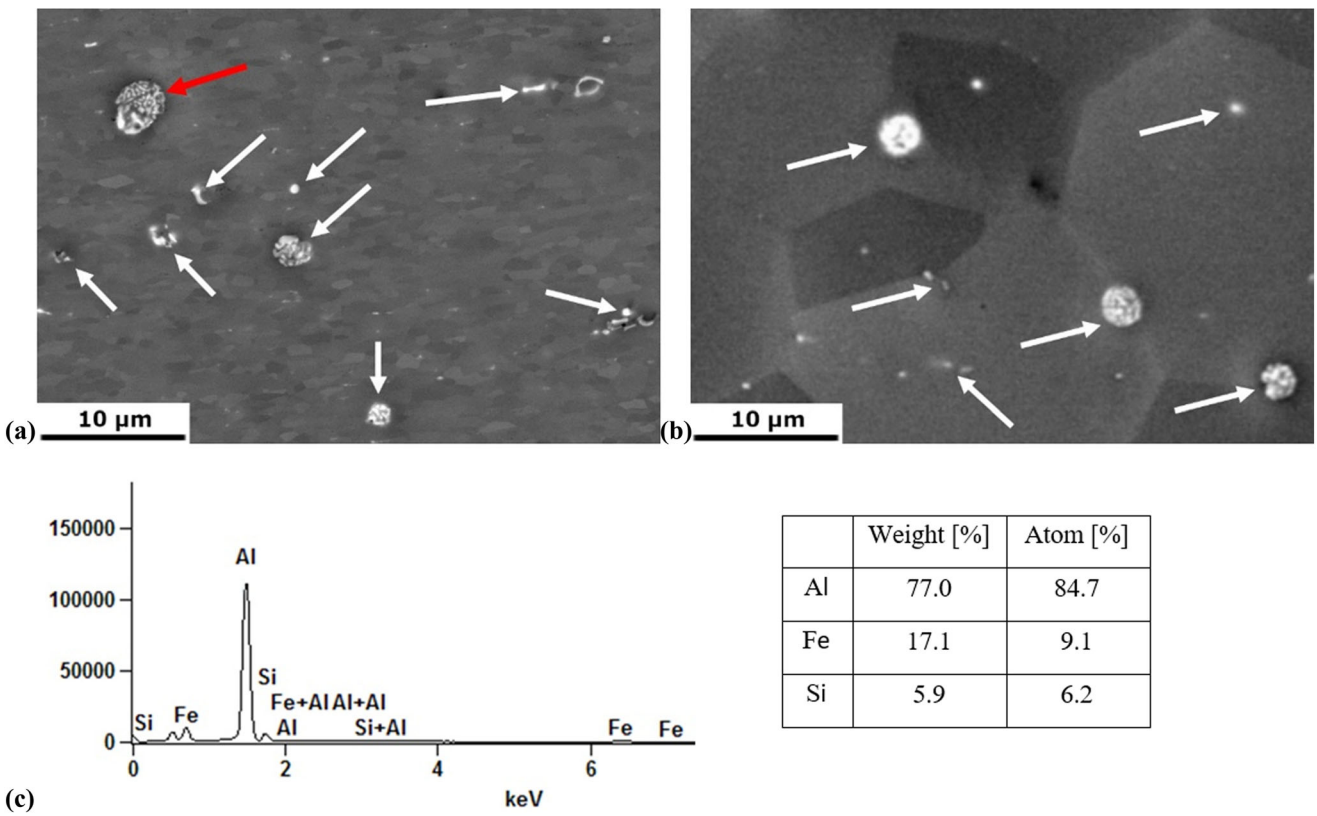

	Weight [%]	Atom [%]
Al	77.0	84.7
Fe	17.1	9.1
Si	5.9	6.2

Figure 7 Microstructure of sample after **a** mtECAP, **b** mtECAP with subsequent annealing at 400 °C, and **c** result of EDX analysis of exemplary primary intermetallic particles (marked by red arrow) together with table showing its composition.

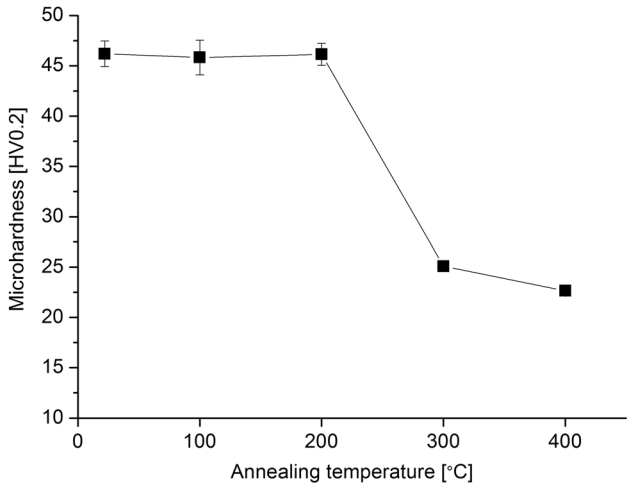

Figure 8 Graph showing the dependence of microhardness on the annealing temperature of the sample after mtECAP.

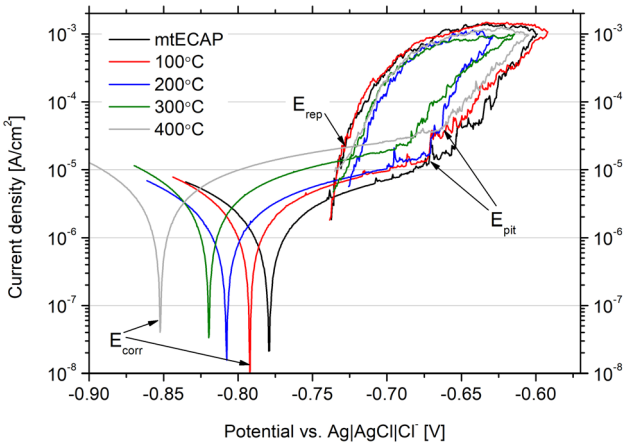

Figure 11 Cyclic potentiodynamic polarization curves for deformed sample and after subsequent annealing.

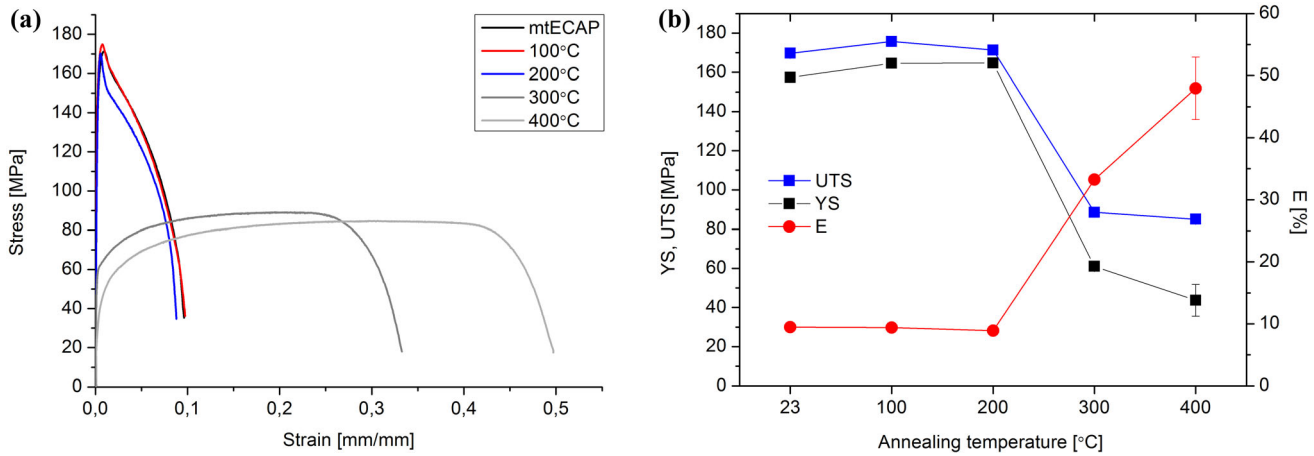

Figure 9 Graphs showing **a** representative tensile curves and **b** the relationship between the yield strength (YS), ultimate tensile strength (UTS), elongation at break (E), and annealing temperature.

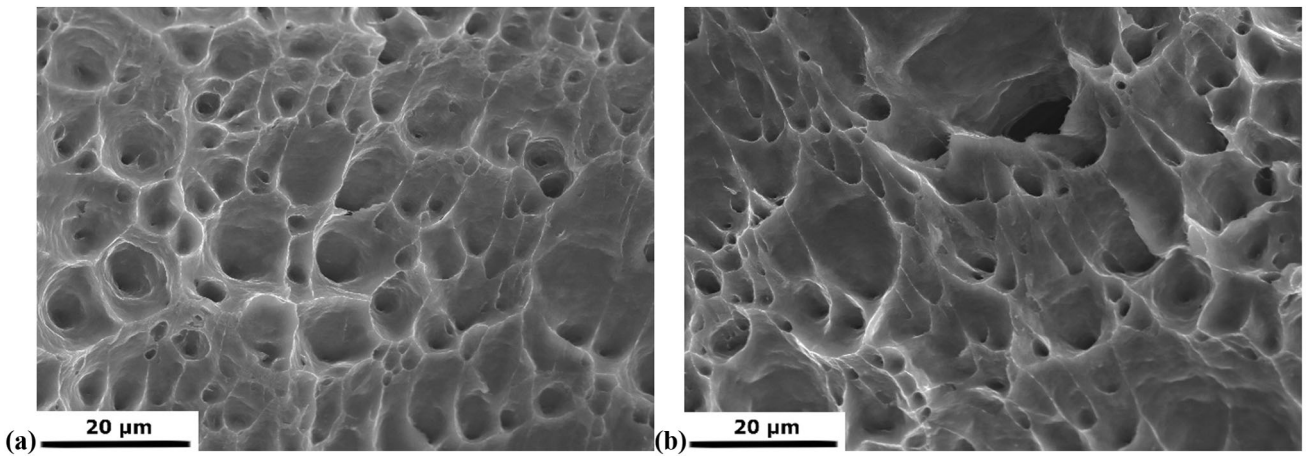

Figure 10 Fractures after static tensile testing for samples after **a** mtECAP process and **b** subsequent annealing at 400 °C.

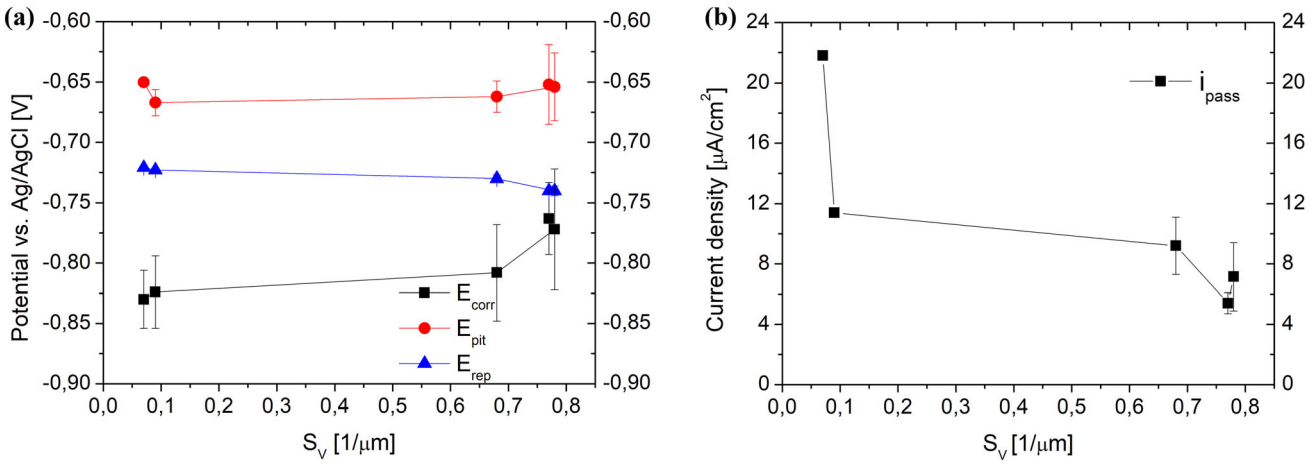

Figure 12 Electrochemical parameters for sample after mtECAP process with subsequent annealing: **a** corrosion potential (E_{corr}), pitting potential (E_{pit}), repassivation potential (E_{rep}), and **b** passive current density (i_{pass}) at 0.7 $V_{(Ag/AgCl)}$.

The average values of the YS and UTS showed the same trend. At 100 °C and 200 °C, even a slight increase in the strength parameters was obtained.

The results for the analysis of fractures indicated their ductile type. Typical images for the two samples with the most significant differences in microstructure, i.e. after the mtECAP process and after subsequent annealing at a temperature of 400 °C, are presented in Fig. 10. Characteristic features for ductile fractures were visible, such as numerous dimples, which have previously been observed for materials after plastic deformation, e.g. for pure copper after ECAP with subsequent cold rolling [38]. The size of the dimples for sample after mtECAP is smaller than for the sample with additional annealing. It can be correlated with the grain size and dislocation density, as these are the preferred locations for the nucleation of microcracks. Hence, there were differences in the size and number of these wells between the samples. The larger dimples were formed as a result of the decohesive mechanism and the smaller ones by the dislocation mechanism. As a result, enhanced dislocation density resulted in a higher number of dimples, as they acted as nuclei for cavity initiation. Therefore, their size was connected with the number of dislocations: with more pronounced grain refinement, the number of dimples increased, as was shown for copper after equal channel angular extrusion [39], where with an increasing number of passes, the number of small dimples increased, while their size decreased.

Corrosion resistance

Potentiodynamic polarization curves recorded in 3.5% NaCl are shown in Fig. 11. The average values of corrosion potential (E_{corr}), pitting potential (E_{pit}), repassivation potential (E_{rep}), and passive current density (i_{pass}) at − 0.7 $V_{(Ag/AgCl)}$ obtained from at least five curves are plotted in Fig. 12, as a function of S_V parameter.

The general shape of all the curves was similar. The most noble E_{corr} was observed for the mtECAP sample, and with increasing annealing temperature, it was shifted towards less noble values. The samples were passive upon exposure to the test solution. The lowest i_{pass} in the passive domain was recorded for the mtECAP sample, and it increased with increasing annealing temperature. The breakdown of the passive film, displayed as an abrupt increase in current density, occurred at potentials higher than − 0.7 $V_{(Ag/AgCl)}$. Generally, the hysteresis loops in the reverse scan were very similar in shape; however, they differed in area. The largest area was noted for the mtECAP sample, while the smallest one was found for the sample annealed at 400 °C, which might indicate that there was a difference in repassivation, and consequently in the morphology of the localized attack, between the samples [19, 20]. Therefore, the shift of E_{corr} towards less noble values and the increase in i_{pass} with increasing annealing temperature indicated that the susceptibility to localized attack increased after annealing.

When the electrochemical parameters are discussed in terms of the S_V factor (see Fig. 12a), it can

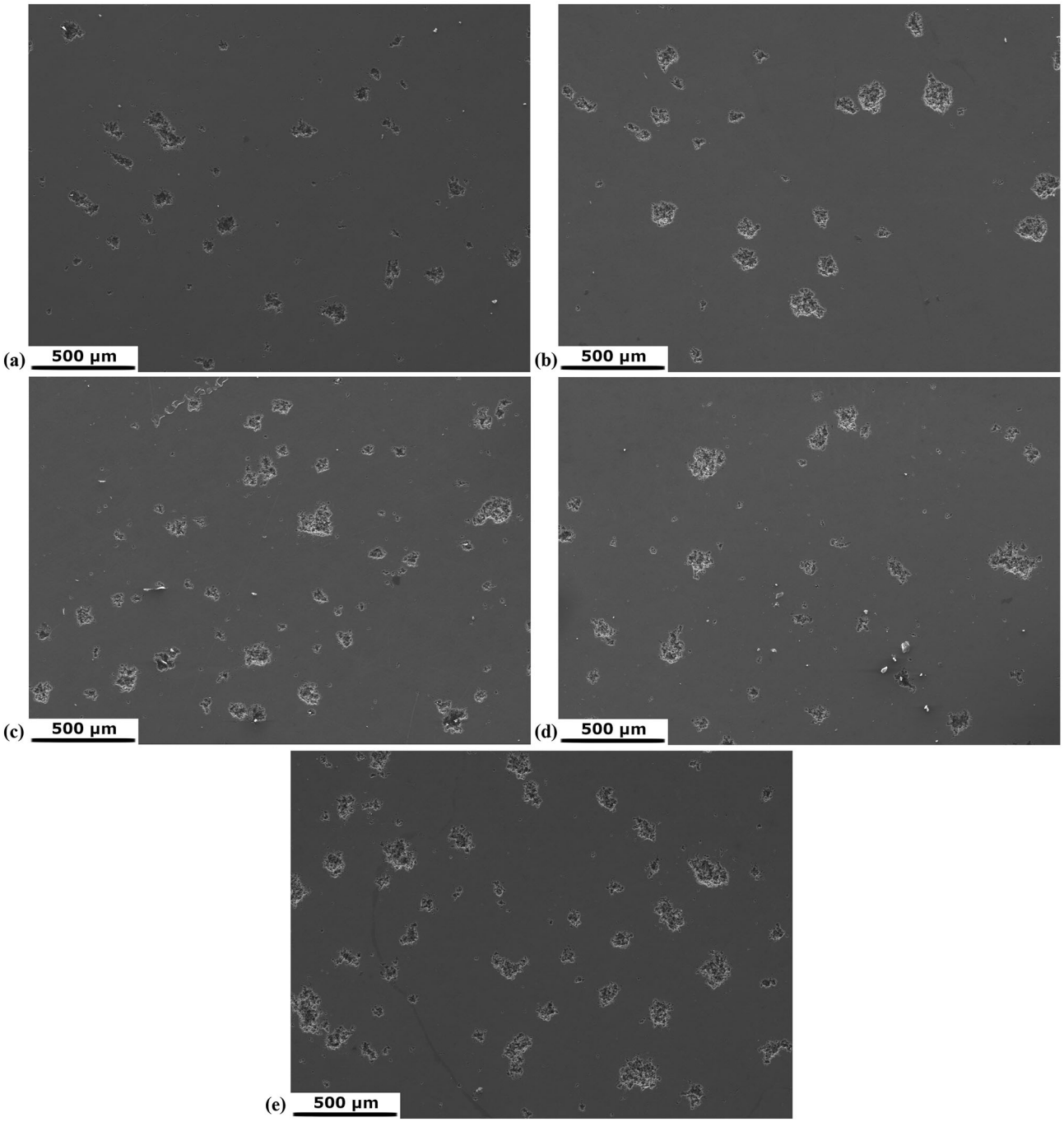

Figure 13 Sample surfaces after potentiodynamic polarization for samples after **a** mtECAP process and with a subsequent annealing at **b** 100 °C, **c** 200 °C, **d** 300 °C, and **e** 400 °C.

be noticed that in general the differences are not significant. However, there is an increase in the E_{pit} and E_{corr} values with the increase in S_V parameter. The most stable and reproducible parameter was repassivation potential (E_{rep}). A slight shift to more noble values was observed for the samples after annealing (lower S_V). In the case of passive current density measured at 0.7 $V_{(Ag/AgCl)}$,the differences are more pronounced. The highest value is observed for the sample with the smallest number of grain boundaries (annealed at 400 °C) and then an abrupt drop is observed. With further increase in S_V, the passive current density further decreases.

The surfaces of the samples after polarization tests are shown in Fig. 13. The observed type of corrosion for all the samples was pitting. The initiation of the pitting has been observed in the vicinity of the intermetallic particles, as seen in Fig. 14. There were visible differences in the number of the pits and the area they occupied. These are presented quantitatively in Fig. 15 by graphs showing firstly the dependence of the surface occupied by the pitting in relation to the total area (A_A) on the annealing temperature, and secondly the dependence of the average size of the pit (d_p) on the annealing temperature. It can be seen that both parameters increased with increasing annealing temperature. In the case of medium-sized pits, there was a significant scattering, shown by the size of error bars on the graph. However, the trend was maintained, and it can be concluded that as the average grain size increased, the corrosion resistance of the material decreased.

Images taken at higher magnification from the surface samples are presented in Fig. 16, showing the crystallographic morphology of the pits. The differences in the dissolution path can be observed as it changed with the annealing temperature. As noted with the mechanical properties, annealing up to 200 °C did not change the morphology of the pits; however, for 300 °C a clear difference could be noted. For the sample after the mtECAP process with subsequent annealing at 300 °C or 400 °C (Fig. 16d, e), crystallographic types of pits can be observed with {100} facets and linked cavities, similar to those described in other studies where the corrosion behaviour of aluminium and its alloys was investigated [40, 41]. In the case of the sample after the mtECAP process and those with annealing at lower temperatures (Fig. 16a–c), the dissolution of the material seemed to be more diverse.

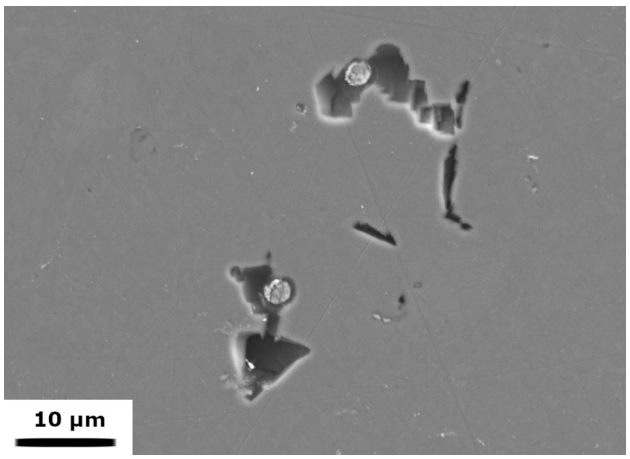

Figure 14 Initiation of pitting corrosion in the vicinity of the intermetallic particles.

Discussion

Effect of annealing on microstructure

Annealing ensures the condition for the occurrence of restoration phenomena by releasing the residual stresses and stored energy of deformed structures. During the annealing of cold-worked metals, the

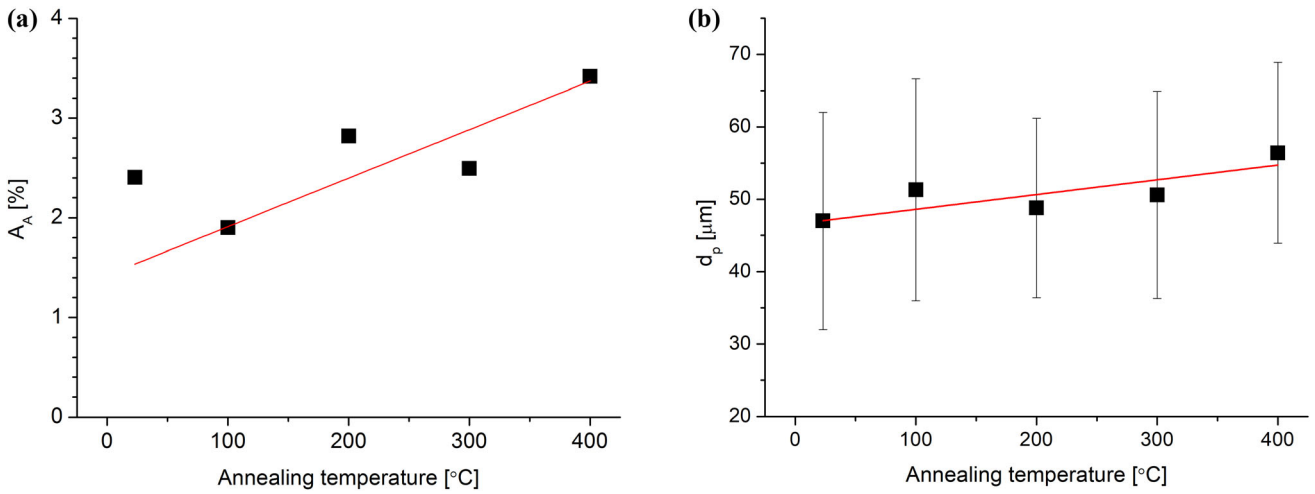

Figure 15 Graphs of the dependence of **a** the surface occupied by pitting in relation to the unit area (A_A) and **b** average pit size (**d**) for samples after the mtECAP process and subsequent annealing temperature.

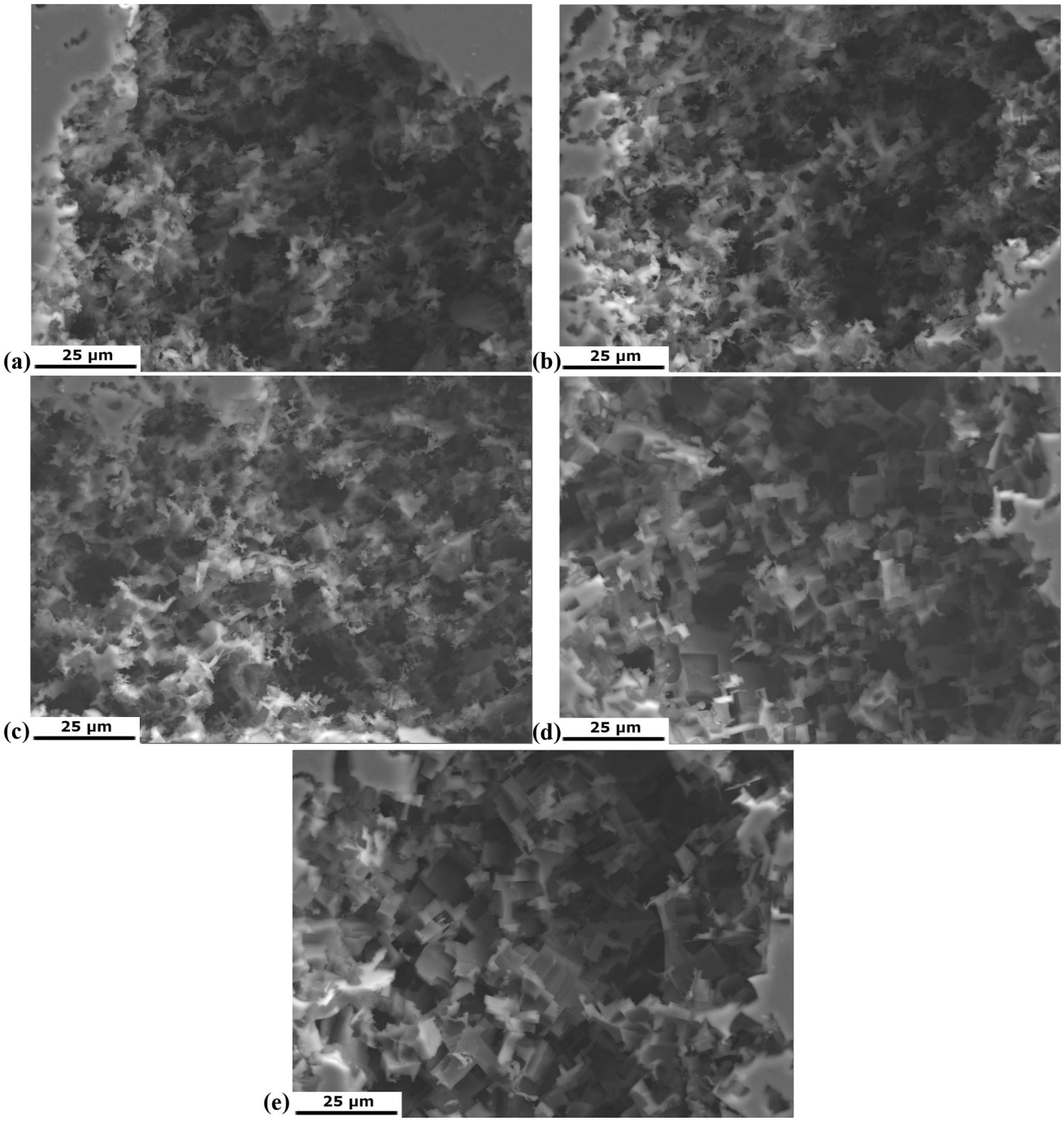

Figure 16 Pit morphology after potentiodynamic tests on a surface of samples after **a** mtECAP process and with a subsequent annealing at **b** 100 °C, **c** 200 °C, **d** 300 °C, and **e** 400 °C.

following processes take place: recovery, recrystallization, and normal/abnormal grain growth [42], which are responsible for a reduction in internal energy. Annealing at lower temperatures causes the rearrangement of dislocations. It can be assumed in the present study that recrystallization was complete before 300 °C, as annealing at this temperature caused selective grain growth (Fig. 5d). This result is in line with results for Al and its alloys in the literature. For 6082 aluminium alloy after cryorolling, recovery occurred between 110 and 250 °C, recrystallization between 250 and 300 °C, and beyond that

grain growth started [43]. For Al–Mn–Si after constrained groove pressing, annealing at 150 °C and 250 °C did not cause any noticeable differences between the obtained microstructures or between the grain sizes. However, annealing at 350 °C caused recrystallization [44]. The observed inhomogeneous and directional grain growth was explained by a strain-induced grain boundary migration phenomenon. This migration was caused by the accumulated strain energy, which was a reason for the formation of new dislocation-free grains. Restoration during annealing at 150 °C promoted residual stress release via dislocation annihilation and subgrain boundary rearrangement caused by crystallite growth. In the present study, the grain growth can be assumed to be homogeneous, since with deformed subgrain structures coarsening occurs through subgrain or grain growth [45].

With the increase in the annealing temperature, most of the stresses inside the deformed material were eliminated, and the dislocations inside the grains moved to the grain boundaries. As a result, the cell structures could be transformed into subgrain boundaries. At an even higher annealing temperature, the grain boundaries became almost free of dislocations and became clear, because the dislocations in the grains rapidly migrated to the small-angle grain boundaries at higher temperatures, rearranged them into dislocation cells, and formed subgrain boundaries by minimizing strain energy. Such changes in microstructure are commonly observed during the annealing of deformed structures and can be clearly observed in the mtECAP samples annealed at 200 °C and 300 °C (Fig. 5c, d). Similar observations were carried out for Al–Mg–Mn–Sc–Zr alloy after cold rolling and annealing up to 400 °C. However, in the case of precipitation-hardenable alloys, second-phase particles may inhibit grain growth [46].

Effect of annealing on mechanical properties

For severely deformed commercially pure aluminium after the ECAP process, annealing at low temperature caused an increase in strength and a decrease in elongation, which was attributed to the recovery of dislocations [47]. In [48], a similar increase in yield strength was observed after annealing at 150–200 °C and was attributed to additional strengthening from the higher amount of HAGBs, which had a stable structure and could act as more effective barriers to moving dislocations. For the material investigated in the present study, an increase in the fraction of HAGBs was obtained with annealing at low temperatures, while the grain size changes were within the error limit (Table 1). These results are similar to those noted in study [49], where in pure aluminium after HPT an anomalous increase in microhardness after annealing was observed, explained by annihilations of the mobile dislocations in the HAGBs, which led to the activation of new dislocation sources during deformation. Also, similar findings were presented for commercially pure aluminium during annealing after cryoECAP processing [50]. Annealing at low temperatures caused an improvement in strength by 20% in commercially pure aluminium initially deformed through the ECAP process [51]. The recovery of dislocations was assumed to be the main cause of annealing strengthening and can also explain an increase in UTS and YS in the present study for samples annealed at 100 °C and 200 °C.

Ultrafine-grained microstructure is not stable at higher temperatures. It has been shown for aluminium and its alloys that thermal stability is preserved up to temperatures of about 200 °C [3]. Annealing at this temperature causes a recovery. When a deformed structure is annealed at a temperature that does not cause recrystallization, typical effects include a coarsening of boundary spacing, a recovery of low angle boundaries, and a reduction in the dislocation density in the grain interior, at grain boundaries, and at triple junctions. In conventional materials with medium to large grain sizes, these changes cause softening by a reduction in dislocation hardening and grain boundary strengthening. However, the changes in the dislocation structure occurring in a nanostructured metal may play a distinct and different role. As a hypothesis, it is suggested that having many dislocation sinks available in the form of closely spaced high-angle boundaries will reduce the number of dislocation sources during annealing. This may lead to an increase in the yield stress in order to activate new dislocation sources during straining. Furthermore, the decrease in the density of interior dislocations that can carry the strain may efficiently reduce the elongation [52].

The softening of metals (e.g. a reduction in microhardness) during recovery is slow and mild. On the

other hand, recrystallization and grain growth are characterized by a faster, more distinct decrease in mechanical properties, as has been shown for Al–Mn alloy [53]. Annealing at 300 °C and 400 °C caused a significant decrease in YS and UTS, which was caused by considerable grain growth, in line with the Hall–Petch equation, which describes the relationship between grain size and strength [54, 55]. It has previously been observed for Al alloys that recrystallization caused a considerable drop in microhardness, as for AA6082 alloy after cryorolling, where annealing at 300 °C led to an abrupt drop in mechanical properties [43].

Effect of annealing on pitting corrosion

A decrease in the corrosion resistance of mtECAP-produced AA1070 aluminium alloy was observed with increasing annealing temperature. Corrosion resistance depends on microstructural features such as grain size, grain boundary distribution, the fraction of HAGBs, dislocation density, and primary intermetallic particles. SPD processing led to significant changes in microstructural features; however, subsequent annealing caused the reorganization of the microstructure and a constant decrease in the number of grain boundaries due to grain coarsening and dislocation annihilation. It is important to note that the annealing did not affect the intermetallics. The intermetallic particles did not undergo any changes during annealing in the present study; therefore, their number was constant for all samples. It was presumed that the initiation of the pitting occurred at the interface between these particles and the Al matrix, as a result of galvanic coupling [56]. Since their number was constant, the number of initiation sites did not change; consequently, other microstructural features affected the resistance to pitting corrosion.

Grain boundaries, triple junctions, and dislocations are the preferred sites of oxidation, and numerous papers show a positive effect of an elevated number of structural defects on corrosion resistance in commercially pure aluminium [57–59]. The multiplication of defects in UFG microstructure accelerates the growth of more compact and stable passive film, which may result in a lower passive current density [14, 60]. The increasing annealing temperature results in the decrease in number of defects, and as a consequence, the number of nucleation sites for passive film is lower which delays the growth of passive film.

The small changes in E_{corr}, E_{rep}, and E_{pit} indicated that the decrease in defect density had a minor effect on these electrochemical parameters. The most significant difference was the shift of E_{corr} to less noble values after annealing. Similar observations were noted for ECAP-processed AA 1050 when compared with the annealed materials [61]. The pitting corrosion resistance showed improvements in E_{pit} average values obtained in potentiodynamic polarization tests; however, the difference in improvement of the mean E_{pit} value between the samples was negligible and was not sequential with each ECAP pass (neither were the intensity and extent of localized corrosive attack). In addition, the corrosion attack was more pronounced for materials with a greater average grain size. Moreover, it was observed that the morphology of corrosion attack changed with increasing annealing temperature, and dissolution occurred along different crystallographic planes. Differences in the dissolution of Al with regard to different planes were also investigated in [62]. It was found that the susceptibility of single crystals to the onset of pitting attack in chloride solution varied in the order {111} > {110} > {100}. This trend was evident from the pitting potential and induction time data, where the most noble pitting potential values and the longest induction periods were recorded for the {100} surface. The resistance of this surface was explained by the differences in the surface energy of the particular planes. Therefore, pit walls are commonly composed of {100} planes, as these planes are slow-dissolving in comparison with the other two planes. However, when the corrosion front reaches a grain boundary, the crystallographic dissolution can be interrupted if fast-dissolving planes are absent from the other side of the grain boundary in the direction of propagation. Such processes can be an explanation for the different morphology of pits for samples after mtECAP, where dissolution occurred more diversely in comparison with samples annealed at 300 °C and 400 °C. More uniform dissolution with no preferred plane was observed for AA2024 alloy during immersion in 3.5 wt% NaCl [63], but the reason for a similar dissolution rates for all three planes was copper enrichment along the pit walls.

Conclusions

In present study, the evolution of pitting corrosion and mechanical properties during annealing of severely deformed commercially pure aluminium has been investigated. Due to applied approach, the influence of primary intermetallic particles, which have a crucial impact on pitting corrosion, has been omitted as their size and distribution did not change during annealing. Based on that other microstructural factors could be investigated. After mtECAP, the AA1070 revealed average grain size of 1.3 μm and a fraction of HAGBs close to 60%. The grain size was stable up to 200 °C, and changes in microstructure consisted of decrease in dislocations density and increase in fraction of HAGBs, which resulted in a slight improvement in mechanical strength. Significant grain growth has been observed for 300 °C and 400 °C, where the average grain size was about 10 μm and 14 μm, respectively. It caused an abrupt decrease in mechanical strength. In the case of electrochemical parameters, it can be concluded that annealing had an impact on corrosion resistance; however, the differences are not significant. Increase in length of grain boundaries and dislocation density resulted in an increase in corrosion and pitting potential, while a decrease in passive current density. The most pronounced changes between samples have been observed in the corrosion attack, as with an increase in the annealing temperature, the size of pits and the surface area damaged increased. Changes in the microstructure due to annealing also changed the morphology of the corrosion attack.

Acknowledgements

The authors would like to acknowledge the financial support from the statutory funds of the Faculty of Materials Science and Engineering, Warsaw University of Technology.

Data availability

The raw/processed data required to reproduce these findings cannot be shared at this time as the data also form part of an ongoing study.

Declarations

Conflict of interest No conflict of interest exists.

Open Access This article is licensed under a Creative Commons Attribution 4.0 International License, which permits use, sharing, adaptation, distribution and reproduction in any medium or format, as long as you give appropriate credit to the original author(s) and the source, provide a link to the Creative Commons licence, and indicate if changes were made. The images or other third party material in this article are included in the article's Creative Commons licence, unless indicated otherwise in a credit line to the material. If material is not included in the article's Creative Commons licence and your intended use is not permitted by statutory regulation or exceeds the permitted use, you will need to obtain permission directly from the copyright holder. To view a copy of this licence, visit http://creativecommons.org/licenses/by/4.0/.

References

[1] Valiev RZ, Estrin Y, Horita Z, Langdon TG, Zehetbauer MJ, Zhu Y (2006) Producing bulk ultrafine-grained materials by severe plastic deformation. Jom 58:33–39. https://doi.org/10.1007/s11837-016-1820-6

[2] Huang Y, Langdon TG (2013) Advances in ultrafine-grained materials. Mater Today 16:85–93. https://doi.org/10.1016/j.mattod.2013.03.004

[3] Hasegawa H, Komura S, Utsunomiya A, Horita Z, Furukawa M, Nemoto M et al (1999) Thermal stability of ultrafine-grained aluminum in the presence of Mg and Zr additions. Mater Sci Eng A 265:188–196. https://doi.org/10.1016/S0921-5093(98)01136-8

[4] Cao WQ, Gu CF, Pereloma EV, Davies CHJ (2008) Stored energy, vacancies and thermal stability of ultra-fine grained copper. Mater Sci Eng A 492:74–79. https://doi.org/10.1016/j.msea.2008.02.048

[5] Godfrey A, Liu Q (2009) Stored energy and structure in top-down processed nanostructured metals. Scr Mater 60:1050–1055. https://doi.org/10.1016/j.scriptamat.2009.02.014

[6] Ralston KD, Birbilis N (2010) Effect of grain size on corrosion: a review. Corrosion 66:1–4. https://doi.org/10.5006/1.3462912

[7] Palumbo G, Thorpe SJ, Aust KT (1990) On the contribution of triple junctions to the structure and properties of nanocrystalline materials. Scr Metall Mater 24:1347–1350. https://doi.org/10.1016/0956-716X(90)90354-J

[8] Balyanov A, Kutnyakova J, Amirkhanova NA, Stolyarov VV, Valiev RZ, Liao XZ et al (2004) Corrosion resistance of ultra fine-grained Ti. Scr Mater 51:225–229. https://doi.org/10.1016/j.scriptamat.2004.04.011

[9] Li T, Liu L, Zhang B, Li Y, Yan F, Tao N et al (2014) Passive behavior of a bulk nanostructured 316L austenitic stainless steel consisting of nanometer-sized grains with embedded nano-twin bundles. Corros Sci 85:331–342. https://doi.org/10.1016/j.corsci.2014.04.039

[10] Liu L, Li Y, Wang F (2008) Influence of grain size on the corrosion behavior of a Ni-based superalloy nanocrystalline coating in NaCl acidic solution. Electrochim Acta 53:2453–2462. https://doi.org/10.1016/j.electacta.2007.10.048

[11] Liu L, Li Y, Wang F (2010) Influence of nanocrystallization on pitting corrosion behavior of an austenitic stainless steel by stochastic approach and in situ AFM analysis. Electrochim Acta 55:2430–2436. https://doi.org/10.1016/j.electacta.2009.11.088

[12] Gupta RK, Singh Raman RK, Koch CC (2012) Electrochemical characteristics of nano and microcrystalline Fe–Cr alloys. J Mater Sci. 47(16):6118–6124. https://doi.org/10.1007/s10853-012-6529-5

[13] Argade GR, Panigrahi SK, Mishra RS (2012) Effects of grain size on the corrosion resistance of wrought magnesium alloys containing neodymium. Corros Sci 58:145–151. https://doi.org/10.1016/j.corsci.2012.01.021

[14] Song D, Ma AB, Jiang JH, Lin PH, Shi J (2011) Improving corrosion resistance of pure Al through ECAP. Corros Eng Sci Technol 46:505–512. https://doi.org/10.1179/147842209X12559428167562

[15] Gollapudi S (2012) Grain size distribution effects on the corrosion behaviour of materials. Corros Sci 62:90–94. https://doi.org/10.1016/j.corsci.2012.04.040

[16] Chan LH, Weiland H, Cheong S, Rohrer GS, Rollett AD (2008) The correlation between grain boundary character and intergrainular corrosion susceptibilility of aluminum alloy. In: Rollett AD (ed) Applications of texture analysis: rollett/applications. Wiley, Hoboken, pp 261–268

[17] Ly R, Hartwig KT, Castaneda H (2018) Effects of strain localization on the corrosion behavior of ultra- fine grained aluminum alloy AA6061. Corros Sci 139:47–57. https://doi.org/10.1016/j.corsci.2018.04.023

[18] Nickel D, Dietrich D, Mehner T, Frint P, Spieler D, Lampke T (2015) Effect of strain localization on pitting corrosion of an AlMgSi0.5 alloy. Metals (Basel) 5(1):172–191

[19] Brunner JG, May J, Höppel HW, Göken M, Virtanen S (2010) Localized corrosion of ultrafine-grained Al–Mg model alloys. Electrochim Acta 55:1966–1970. https://doi.org/10.1016/j.electacta.2009.11.016

[20] Brunner JG, Birbilis N, Ralston KD, Virtanen S (2012) Impact of ultrafine-grained microstructure on the corrosion of aluminium alloy AA2024. Corros Sci 57:209–214. https://doi.org/10.1016/j.corsci.2011.12.016

[21] Birbilis N, Buchheit RG (2005) Electrochemical characteristics of intermetallic phases in aluminum alloys. J Electrochem Soc 152:B140–B151. https://doi.org/10.1149/1.1869984

[22] Adamczyk-Cieślak B, Mizera J, Kurzydłowski KJ (2011) Microstructures in the 6060 aluminium alloy after various severe plastic deformation treatments. Mater Charact 62:327–332. https://doi.org/10.1016/j.matchar.2011.01.009

[23] Chung MK, Choi YS, Kim JG, Kim YM, Lee JC (2004) Effect of the number of ECAP pass time on the electrochemical properties of 1050 Al alloys. Mater Sci Eng A 366:282–291. https://doi.org/10.1016/j.msea.2003.08.056

[24] Seri O, Furumata K (2002) Effect of Al–Fe–Si intermetallic compound phases on initiation and propagation of pitting attacks for aluminum 1100. Mater Corros 53:111–120. https://doi.org/10.1002/1521-4176(200202)53:2

[25] Akiyama E, Zhang Z, Watanabe Y, Tsuzaki K (2009) Effects of severe plastic deformation on the corrosion behavior of aluminum alloys. J Solid State Electrochem 13:277–282. https://doi.org/10.1007/s10008-007-0496-9

[26] Korchef A, Kahoul A (2013) Corrosion behavior of commercial aluminum alloy processed by equal channel angular pressing. Int J Corros 2013:1–11

[27] Laurino A, Andrieu E, Harouard JP, Lacaze J, Lafont MC, Odemer G et al (2013) Corrosion behavior of 6101 aluminum alloy strands for automotive wires. J Electrochem Soc 160:C569–C575

[28] Raab GI (2005) Plastic flow at equal channel angular processing in parallel channels. Mater Sci Eng A 410–411:230–233. https://doi.org/10.1016/j.msea.2005.08.089

[29] Olejnik L, Rosochowski A (2005) Methods of fabricating metals for nano-technology. Bull Polish Acad Sci 53:413–423

[30] Olejnik L, Rosochowski A (2008) Scaled-up ECAP with enhanced productivity. Steel Res Int 2:439–446

[31] Rosochowski A, Olejnik L (2002) Numerical and physical modelling of plastic deformation in 2-turn equal channel angular extrusion. J Mater Process Technol 125–126:309–316. https://doi.org/10.1016/S0924-0136(02)00339-4

[32] Valiev RZ, Langdon TG (2006) Principles of equal-channel angular pressing as a processing tool for grain refinement. Prog Mater Sci 51:881–981. https://doi.org/10.1016/j.pmatsci.2006.02.003

[33] Sander G, Thomas S, Cruz V, Jurg M, Birbilis N, Gao X et al (2017) On The corrosion and metastable pitting characteristics of 316l stainless steel produced by selective laser melting. J Electrochem Soc 164:C250–C257. https://doi.org/10.1149/2.0551706jes

[34] Molak RM, Kartal ME, Pakiela Z, Kurzydlowski KJ (2016) The effect of specimen size and surface conditions on the local mechanical properties of 14MoV6 ferritic – pearlitic steel. Mater Sci Eng A 651:810–821. https://doi.org/10.1016/j.msea.2015.11.037

[35] Prangnell PB, Bowen JR, Apps PJ (2004) Ultra-fine grain structures in aluminium alloys by severe deformation processing. Mater Sci Eng A 375–377:178–185. https://doi.org/10.1016/j.msea.2003.10.170

[36] Muzyk M, Pakiela Z, Kurzydlowski KJ (2011) Ab initio calculations of the generalized stacking fault energy in aluminium alloys. Scr Mater 64:916–918. https://doi.org/10.1016/j.scriptamat.2011.01.034

[37] Mishin OV, Godfrey A, Juul Jensen D, Hansen N (2013) Recovery and recrystallization in commercial purity aluminum cold rolled to an ultrahigh strain. Acta Mater 61(4):5354–5364. https://doi.org/10.1016/j.actamat.2013.05.024

[38] Ranjbar Bahadori S, Dehghani K, Bakhshandeh F (2013) Microstructure, texture and mechanical properties of pure copper processed by ECAP and subsequent cold rolling. Mater Sci Eng A 583:36–42. https://doi.org/10.1016/j.msea.2013.06.061

[39] Higuera-Cobos OF, Cabrera JM (2013) Mechanical, microstructural and electrical evolution of commercially pure copper processed by equal channel angular extrusion. Mater Sci Eng A 571:103–114. https://doi.org/10.1016/j.msea.2013.01.076

[40] Moore KL, Sykes JM, Grant PS (2008) An electrochemical study of repassivation of aluminium alloys with SEM examination of the pit interiors using resin replicas. Corros Sci 50:3233–3240. https://doi.org/10.1016/j.corsci.2008.08.027

[41] Ambat R, Davenport AJ, Scamans GM, Afseth A (2006) Effect of iron-containing intermetallic particles on the corrosion behaviour of aluminium. Corros Sci 48:3455–3471. https://doi.org/10.1016/j.corsci.2006.01.005

[42] Humphreys FJ, Hatherly M (1996) Recrystallization and related annealing phenomena. Pergamon, Oxford, pp 327–362

[43] Kumar N, Rao PN, Jayaganthan R, Brokmeier H (2015) Effect of cryorolling and annealing on recovery, recrystallisation, grain growth and their influence on mechanical and corrosion behaviour of 6082 Al alloy. Mater Chem Phys 165:177–187. https://doi.org/10.1016/j.matchemphys.2015.09.014

[44] Pouraliakbar H, Jandaghi MR, Khalaj G (2017) Constrained groove pressing and subsequent annealing of Al–Mn–Si alloy: microstructure evolutions, crystallographic transformations, mechanical properties, electrical conductivity and corrosion resistance. Mater Des 124:34–46. https://doi.org/10.1016/j.matdes.2017.03.053

[45] Yu T, Hansen N (2016) Coarsening kinetics of fine-scale microstructures in deformed materials. Acta Mater 120:40–45. https://doi.org/10.1016/j.actamat.2016.08.032

[46] Tang Z, Jiang F, Long M, Jiang J, Liu H, Tong M (2020) Effect of annealing temperature on microstructure, mechanical properties and corrosion behavior of Al–Mg–Mn–Sc–Zr alloy. Appl Surf Sci 514:1–12. https://doi.org/10.1016/j.apsusc.2020.146081

[47] Ren J, Shan A (2010) Strengthening and stress drop of ultrafine grain aluminum after annealing. Trans Nonferrous Met Soc China 20:2139–2142

[48] Cao Y, He L, Zhou Y, Wang P, Cui J (2016) Contributions to yield strength in an ultrafine grained 1050 aluminum alloy after DC current annealing. Mater Sci Eng A 674:193–202. https://doi.org/10.1016/j.msea.2016.06.084

[49] Mavlyutov AM, Bondarenko AS, Murashkin MY, Boltynjuk EV, Valiev RZ, Orlova TS (2017) Effect of annealing on microhardness and electrical resistivity of nanostructured SPD aluminium. J Alloys Compd 698:539–546. https://doi.org/10.1016/j.jallcom.2016.12.240

[50] Cao Y, He L, Zhang L, Zhou Y, Wang P, Cui J (2016) Evolution of mechanical properties of ultrafine grained 1050 alloy annealing with electric current. Mater Charact 113:160–167. https://doi.org/10.1016/j.matchar.2016.01.007

[51] Jiang-wei R, Ai-dang S (2010) Strengthening and stress drop of ultrafine grain aluminum after annealing. Trans Nonferrous Met Soc China 20:2139–2142. https://doi.org/10.1016/S1003-6326(09)60431-3

[52] Huang X, Hansen N, Tsuji N (2006) Hardening by annealing and softening by deformation in nanostructured metals. Science 312(5771):249–251. https://doi.org/10.1126/science.1124268

[53] Kang HG, Lee JP, Huh MY, Engler O (2008) Stability against coarsening in ultra-fine grained aluminum alloy AA 3103 sheet fabricated by continuous confined strip shearing. Mater Sci Eng A 486:470–480. https://doi.org/10.1016/j.msea.2007.09.048

[54] Hall EO (1951) The deformation and ageing of mild steel: III discussion of results. Proc Phys Soc Sect B 64:747. https://doi.org/10.1088/0370-1301/64/9/303

[55] Petch NJ (1953) The cleavage strength of polycrystals. J Iron Steel Inst 174:25–28. https://doi.org/10.1007/BF01972547

[56] Orłowska M, Ura-Bińczyk E, Olejnik L, Lewandowska M (2019) The effect of grain size and grain boundary misorientation on the corrosion resistance of commercially pure aluminium. Corros Sci 148:57–70. https://doi.org/10.1016/j.corsci.2018.11.035

[57] Ralston KD, Fabijanic D, Birbilis N (2011) Effect of grain size on corrosion of high purity aluminium. Electrochim Acta 56:1729–1736. https://doi.org/10.1016/j.electacta.2010.09.023

[58] Abdulstaar M, Mhaede M, Wagner L, Wollmann M (2014) Corrosion behaviour of Al 1050 severely deformed by rotary swaging. Mater Des 57:325–329. https://doi.org/10.1016/j.matdes.2014.01.005

[59] Song D, Ma AB, Jiang JH, Lin PH, Yang DH (2009) Corrosion behavior of ultra-fine grained industrial pure Al fabricated by ECAP. Trans Nonferrous Met Soc China 19(5):1065–1070. https://doi.org/10.1016/S1003-6326(08)60407-0

[60] Wang X, Nie M, Wang CT, Wang SC, Gao N (2015) Microhardness and corrosion properties of hypoeutectic Al–7Si alloy processed by high-pressure torsion. Mater Des 83:193–202. https://doi.org/10.1016/j.matdes.2015.06.018

[61] Quartiermeister MV, Magalhães DCC, Braga DP, Silva R, Rovere CAD (2020) On the pitting corrosion behavior of ultrafine–grained aluminum processed by ECAP: a statistical analysis. Mater Corros 71(8):1244–1256. https://doi.org/10.1002/maco.201911293

[62] Treacy GM, Breslin CB (1998) Electrochemical studies on single-crystal aluminium surfaces. Electrochim Acta 43(12–13):1715–1720

[63] Zhang X, Zhou X, Hashimoto T, Liu B (2017) Localized corrosion in AA2024-T351 aluminium alloy: transition from intergranular corrosion to crystallographic pitting. Mater Charact 130:230–236. https://doi.org/10.1016/j.matchar.2017.06.022

Publisher's Note Springer Nature remains neutral with regard to jurisdictional claims in published maps and institutional affiliations.